

Collective motion of driven semiflexible filaments tuned by soft repulsion and stiffness

Jeffrey M. Moore,¹ Tyler N. Thompson,¹ Matthew A. Glaser,¹ and Meredith D. Betterton^{1,2}

¹*Department of Physics, University of Colorado, Boulder, CO 80309*

²*Department of Molecular, Cellular, and Developmental Biology, University of Colorado, Boulder, CO 80309*

(Dated: March 26, 2022)

In active matter systems, self-propelled particles can self-organize to undergo collective motion, leading to persistent dynamical behavior out of equilibrium. In cells, cytoskeletal filaments and motor proteins exhibit activity and self-organization into complex structures important for cell mechanics, motility, and division. Collective dynamics of cytoskeletal systems can be reconstituted using filament gliding experiments, in which cytoskeletal filaments are propelled by surface-bound motor proteins. These experiments have observed diverse behavior, including flocks, polar streams, swirling vortices, and single filament spirals. Recent experiments with microtubules and kinesin motor proteins found that the effective repulsive interaction between filaments can be tuned by crowding agents in solution, altering the collective behavior. Adding a crowder reduced filament crossing, promoted alignment, and led to a transition from active, isotropically oriented filaments to locally aligned polar streams. These results suggest that tunable soft repulsion can control active phase behavior, but how altering steric interactions and filament stiffness alter collective motion is not fully understood. Here we use simulations of driven filaments with tunable soft repulsion and rigidity in order to better understand how the interplay between filament flexibility and steric effects can lead to different active steady states. We identify swirling flocks, polar streams, buckling bands, and spirals, and describe the physics that govern transitions between these states. In addition to repulsion, tuning filament stiffness can promote collective behavior, and controls the transition between active isotropic filaments, locally aligned flocks, and polar streams.

Interacting active particles exhibit complex and dynamical order at length scales much larger than the scale of a single particle. Collective dynamics are common for living systems, including swimming bacteria, schools of fish, flocks of birds, and crowds of people [1–6]. The study of collective behavior in systems of active biopolymers is motivated by the activity of living cells, because intracellular organization and dynamics are largely governed by an active filament network called the cytoskeleton. Interactions between cytoskeletal filaments and motor proteins generate active forces that control the assembly of critical cellular structures and long-range patterns [7–9], or turbulent 2D active nematics [10, 11]. One method for studying the collective behavior of active matter is filament gliding experiments, wherein cytoskeletal filaments are propelled by motor proteins bound to a surface. Previous work on filament gliding has reported several nonequilibrium steady states, including long-range polar streams, lattices of nematic vortices, and frozen, active steady states of rotating spools [12–17]. However, our understanding of the physics that controls these phases is incomplete.

Although many filament gliding experiments exhibit collective behavior, systems of microtubules propelled by kinesin motors often do not interact and align sufficiently for the emergence of collective motion [15, 16, 18]. Recent work showed that adding a molecular crowding agent (methylcellulose) can reduce filament crossing and cause microtubules to sterically interact and locally align, leading to collective motion [18–20]. Similar behavior was also recently observed in actomyosin motility experiments, where the presence of a crowding agent increased

filament alignment interactions [17]. This transition has been proposed to occur due to an attractive depletion force between filaments, leading to an increase in steric effects, which promote alignment [11, 17–20]. As a result, the collective dynamics of gliding filaments can be tuned by depletant concentration, with high concentration driving a transition from non-interacting, isotropically oriented filaments to polar streams of aligned filaments. However, the underlying physics contributing to the collective motion observed in these experiments is not well understood. Previous work investigating collective behavior of active polar filaments includes Vicsek-type models of self-propelled polar particles [21–25], numerical simulations of driven rigid rods [26–30] and elastic filaments with fixed interaction potential [31, 32]. Although much has been learned about the conditions contributing to the dynamic behavior of active filaments, previous models did not explore how the phase behavior changes with varying rigidity and tunable interaction strength.

In this paper, we study the non-equilibrium phase behavior of driven semiflexible filaments that interact with a tunable soft repulsive potential. The steady-state behavior depends both on the strength of the repulsive potential and filament rigidity. The phases observed include active filaments that are isotropically oriented and disordered, locally aligned flocks, long polar streams, and self-interacting filament spirals. Increasing the repulsion leads to a transition between active isotropic filaments and aligned polar streams, in agreement with experiment. However, we also find that increasing filament rigidity promotes collective motion, which is counterintuitive because higher rigidity lowers the probability that

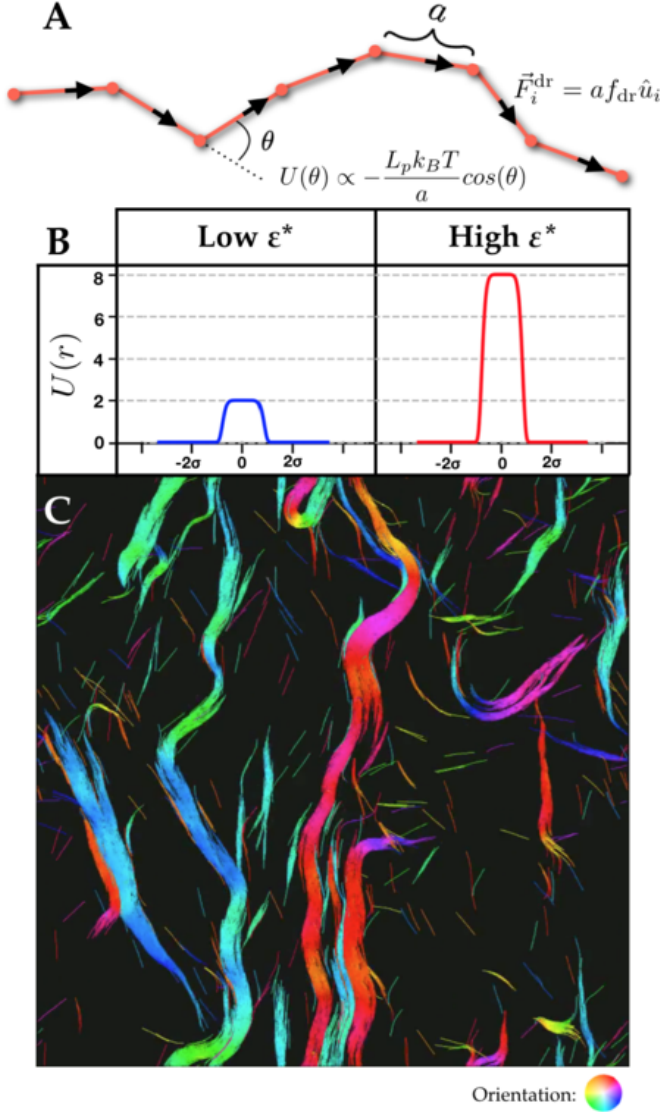


FIG. 1. A) Schematic of the model of self-propelled, inextensible, semiflexible filaments. Each filament consists of rigid segments of length a with an energy for bending two adjacent segments $U(\theta)$. Each segment experiences a parallel driving force F_{dr} , resulting in a self-propulsion force tangent to the contour of the filament. B) Plot depicting the filament interaction potential $U(r)$ centered on a filament of diameter σ , plotted with dimensionless units ϵ^* . C) Snapshot of a simulation of many filaments, with packing fraction $\phi = 0.2$, filament rigidity $\kappa = 100$, and interaction energy $\epsilon^* = 5.6$.

two intersecting filaments align [33]. Therefore, we propose that while filament alignment by collisions is important, the degree of filament orientational persistence (controlled by stiffness) is an additional key physical effect for collective motion. Our results suggest that alignment interactions from collisions are not solely responsible for the emergence of collective behavior in active filament systems.

Our simulation model expands our previous work on

Brownian polar filaments with repulsive interactions by adding semiflexibility [30, 34, 35]. Each filament is a discretized inextensible worm-like chain composed of finite rigid segments (Fig. 1A, [33]). Neighboring segments on a chain experience a restorative bending force determined by the filament persistence length (L_p) and the angle between the segments. Each segment of the filament experiences random forces so that its dynamics obey the fluctuation-dissipation theorem for slender filaments at thermal equilibrium [36]. Our simulations implement the algorithm of Montesi, Morse, and Pasquali for a bead-rod semiflexible chain with anisotropic friction [37]. The activity due to the motor proteins is modeled by a polar driving force per unit length f_{dr} parallel to each filament segment. This choice reflects experimental observations that filament velocity is constant, even during filament crossing events [15], suggesting that stochastic effects due to the motors (e.g., binding and unbinding, variation in motor stepping) occur at short enough time scales so as to not significantly alter large-scale behavior.

Interactions between filaments are purely repulsive but soft, defined by the generalized exponential model potential (GEM-8) between segments, $U(r) = \epsilon e^{-(r/\sigma)^\xi}$, with cutoff $U(r > \sqrt{2}\sigma) = 0$. Here r is the minimum distance between neighboring segments and σ the diameter of a filament (Fig. 1B). The maximum potential value ϵ represents the energy required for two segments to overlap. This potential is steep near the edge of a filament, modeling the interactions tuned by the concentration of crowding agents. Interactions occur between each filament segment, except for nearest-neighbor segments of the same filament. While filaments experience local drag, we neglect long-range hydrodynamic interactions because previous experiments found these forces to be negligible [19].

To start the simulation, filaments are inserted at a packing fraction $\phi = A_{\text{fil}}/A_{\text{sys}}$, where A_{sys} is the area of the simulation box and $A_{\text{fil}} = N(L\sigma + \pi\sigma^2)$ is the total area occupied by N spherocylindrical filaments of length L and diameter σ . The characteristic timescale is the time for a filament to move the distance of its contour length, $\tau_A = L/v$, with the velocity depending on the total driving force and the coefficient of friction acting parallel to the filament, $v = \xi_{\parallel}^{-1} F_{\text{dr}}$. The filament driving force per unit length is set by the Péclet number, which is the ratio of active and diffusive transport time scales,

$$Pe = \frac{\tau_D}{\tau_A} = \frac{L^2 \xi_{\parallel} / k_B T}{\xi_{\parallel} / f_{\text{dr}}} = \frac{f_{\text{dr}} L^2}{k_B T}. \quad (1)$$

We set $Pe = 10^5$ to study highly driven systems, based on calculations of active forces in experiments [15]. Simulations were run for $10^3 - 10^4 \tau_A$, depending on the relaxation time for the particular phase of the system.

Our results depend on five dimensionless parameters: filament rigidity $\kappa = L_p/L$, interaction energy $\epsilon^* = \epsilon/\epsilon_{\text{dr}}$,

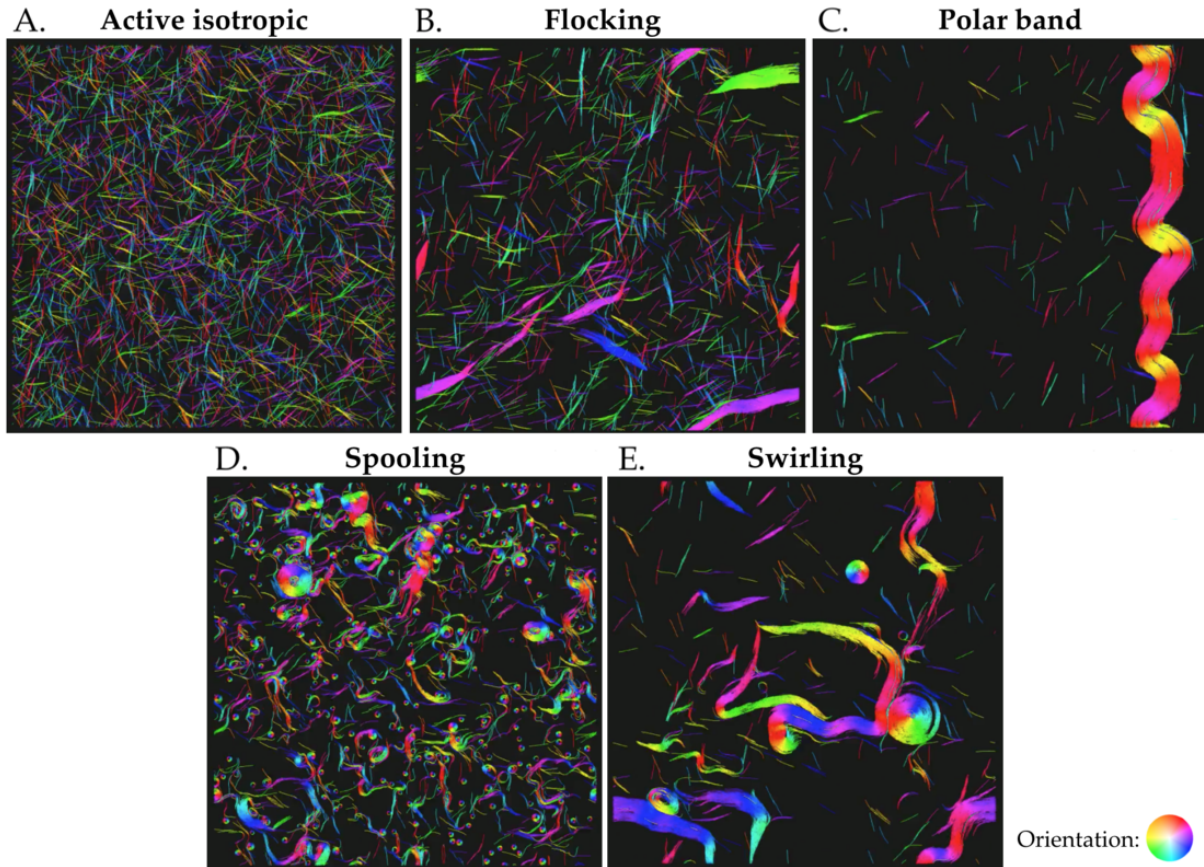


FIG. 2. Snapshots of the characteristic dynamical phases in our simulations. A) Active isotropic ($\phi = 0.2$, $\epsilon^* = 1.4$, $\kappa = 50$). B) Flocking ($\phi = 0.2$, $\epsilon^* = 1.9$, $\kappa = 100$). C) Polar band ($\phi = 0.2$, $\epsilon^* = 4.7$, $\kappa = 100$). D) Spooling ($\phi = 0.2$, $\epsilon^* = 9.3$, $\kappa = 20$). E) Swirling ($\phi = 0.2$, $\epsilon^* = 9.3$, $\kappa = 100$).

packing fraction $\phi = A_{\text{fil}}/A_{\text{sys}}$, filament aspect ratio $l = L/\sigma = 60$, system size $l_{\text{sys}} = L_{\text{sys}}/L = 20$, and Péclet number. The interaction energy has been rescaled by ϵ_{dr} , which is the energy required for the GEM-8 interaction potential to exert a maximum force that cancels the driving force of a particle with length σ , such that $\epsilon^* = l$ would lead to effectively impenetrable filaments for a given Péclet number. In order to determine how collective behavior emerges in systems of driven filaments with tunable interactions, filament stiffness, and density, we varied ϵ^* , κ , and ϕ . The interaction potential strength ϵ^* varied from 0.93–9.3. Filament density and rigidity were $\phi = 0.04, 0.1, 0.2$, and 0.4 and $\kappa = 20, 50$, and 100 . Although the filament aspect ratio is fixed in our simulations, varying the filament rigidity is analogous to varying the length of a filament with a fixed persistence length and vice versa.

To quantify the dynamical phases, we used six order parameters: the global polar order P , global nematic order Q , contact number c , local polar order p , positional order $S(q_0)$, and spiral number s [33]. The global polar order is the magnitude of the steady-state average orien-

tation vector of gliding filaments, and is large if filaments are globally aligned and oriented. The global nematic order is the largest eigenvalue of the 2D nematic order tensor, indicating the degree of orientational alignment. The local polar order measures the local alignment of filaments with their distance-weighted neighbors, and can be large even in the absence of global polar order. Following our previous work, we determine a filament to be in a flocking state when its average local polar order parameter exceeds the threshold $p = 0.5$ [30]. The contact number is a measure of the average number of nearest neighbors for each segment. The positional order parameter is derived from the structure factor, indicating the degree of pattern regularity in the filament organization [33]. The spiral number measures average filament shape, with a straight filament having $s = 0$ and a filament bent into a perfect circle having $s = 1$ [33].

Our simulations generated five primary phases: active isotropic, flocking, banding, swirling, and spooling (Fig. 2). In the active isotropic phase, filaments cross each other in all directions, resembling filament gliding experiments that do not exhibit collective motion

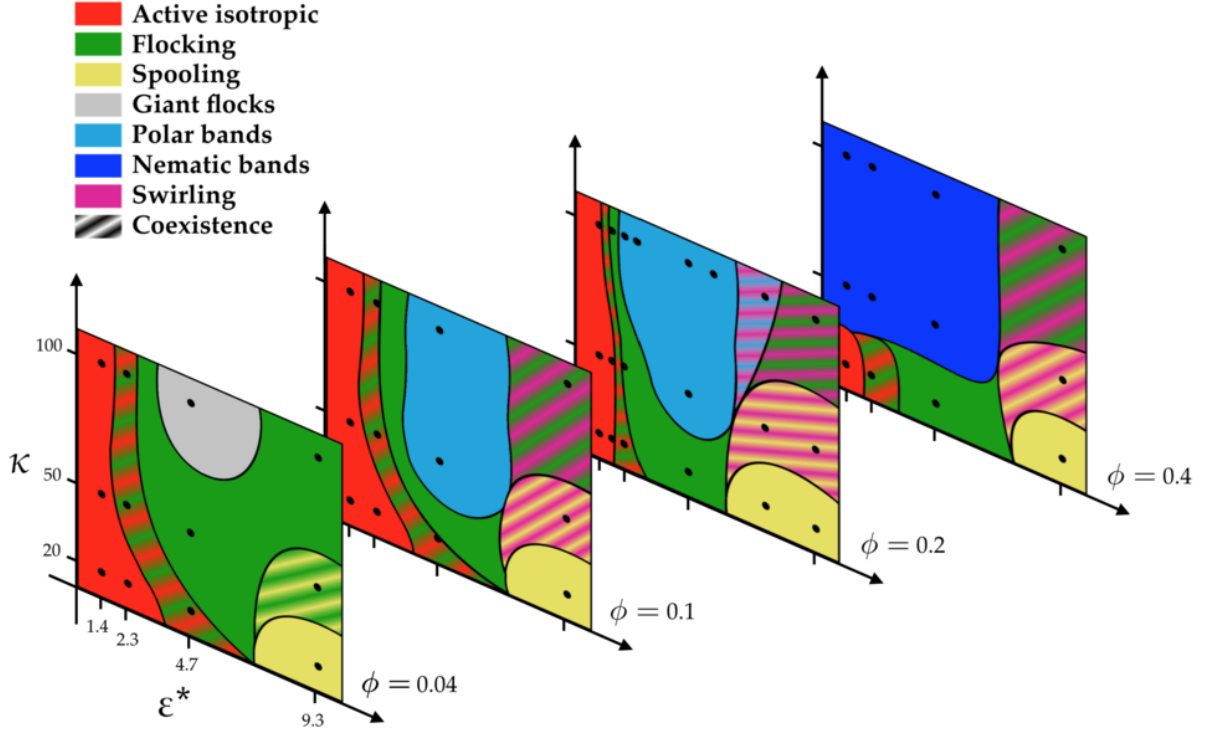


FIG. 3. Phase diagram of self-propelled semiflexible filaments with varying filament rigidity L_p/L , interaction energy ϵ , and packing fraction ϕ . Phase boundaries are predicted using a support vector machine classification algorithm with a Gaussian kernel centered at each of the labeled points at which simulation data are available (indicated on the diagram as black circles), with kernel amplitude and variance chosen for boundary smoothness [33].

(Fig. 2A, [33]). The flocking phase is characterized by polar domains of aligned filaments (Fig. 2B), and can be stable as one large flock (giant flock phase) or with multiple coexisting flocks (flocking phase). Flocks are dynamic, with filaments continuously joining and leaving the flocking state. The banding phase occurs when most filaments join a stable band of filaments that spans the system length (Fig. 2C), and can be either one band (polar band phase) or many counter-propagating bands (nematic band phase). In the spooling phase, filaments are flexible enough to self-interact, and many filaments form spirals (Fig. 2D). The swirling phase contains large, swarming flocks that collide, self-interact, and form transient vortices (Fig. 2E).

Collective motion emerges with increasing repulsion or rigidity. When both filament repulsion and rigidity are small, we find the active isotropic phase at all densities (Fig. 3). Self-organization and collective motion can occur by increasing either ϵ^* or κ ; increasing ϵ^* tends to increase collective behavior, while increasing κ or ϕ tends to increase long-range order. Remarkably, there are regions of phase space where increasing κ drives the emergence of collective motion, and regions where increasing ϵ^* abolishes collective behavior by lowering long-range organization.

Previous experimental work found that the transition from an active isotropic phase to polar streams was driven by an increase in alignment events between pairs of colliding filaments [16, 18–20]. Filament crossing events occur when intersecting filaments continue along their previous trajectories unperturbed, which occurs with probability $P_{\text{cross}} = 1 - P_{\text{align}}$. We find that increasing ϵ^* increases P_{align} and collective motion, in agreement with experiments [18–20]. Therefore, it was surprising that increasing the filament rigidity κ decreases P_{align} , yet increases filament collective motion (Fig. 4).

The counter-intuitive result that increasing stiffness lowers collisional alignment but increases collective motion appears to reflect a trade-off between filament crossing and the orientational persistence of filament trajectories. We measured the time autocorrelation of filament orientation, which is higher when gliding filaments have more ballistic trajectories. Longer correlation time occurs when κ is larger, because filaments resist deflection, and is correlated with collective dynamics [33]. Flocking filaments that move ballistically have longer-lived alignment, resulting in more filaments joining the flock than leaving it. In other words, more flexible filaments re-orient more, so fewer filaments can join the flock, and thus the system requires a larger ϵ^* to cross the active

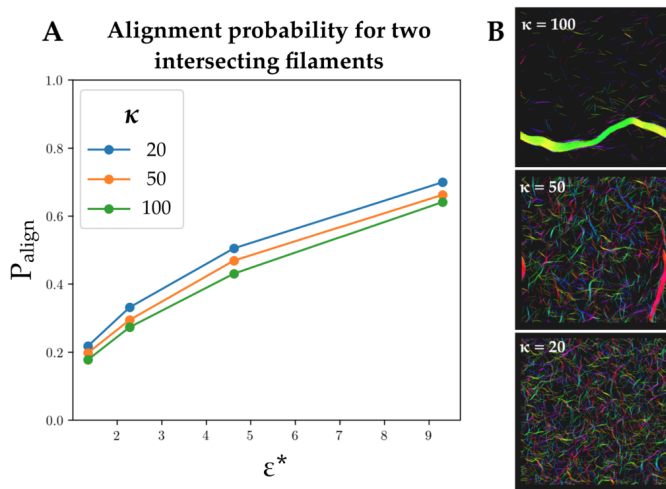


FIG. 4. A) Plot of the probability for two intersecting filaments to align relative to each other upon collision. Increasing the interaction potential strength ϵ^* increases P_{align} while increasing filament rigidity κ decreases it. Nevertheless, increasing κ also increases collective motion of gliding filaments. B) Simulation snapshots illustrating how increasing filament rigidity increases collective motion of gliding filaments. All images are simulations with fixed interaction potential strength, $\epsilon^* = 4.7$.

isotropic–flocking boundary. This occurs even though increasing flexibility increases P_{align} . Therefore, our results suggest that both filament alignment and persistent filament orientation during movement contribute to collective motion and stable flocks (Fig. 4).

In the active isotropic phase, filaments rarely align upon collision, and do not stay aligned when they do. Filaments are thus randomly oriented and uncorrelated with other filaments on average (Fig. 5A). Near the active isotropic–flocking transition, filaments briefly align when they collide at acute angles, but do not stay aligned long enough for more filaments to join the pair, preventing flock formation. This alignment lifetime–alignment probability interplay controls whether collective motion occurs. Increasing κ at low interaction potential strengths ($\epsilon^* = 1.4\text{--}4.7$) decreases the absolute number of filament alignment events, but increases the alignment lifetime, allowing flock formation (Fig. 5B).

At steady state, the flocking phase may consist of multiple polar domains of aligned filaments, or all flocks may merge. At moderate density ($\phi = 0.1, 0.2$), flock coalescence results in a giant flock that spans the length of the system ($L_{\text{flock}} > l_{\text{sys}}$), forming a stable, polar band. At high density ($\phi = 0.4$), multiple independent bands can form simultaneously, resulting in the nematic band phase. We note that high filament density paired with high κ results in more collective motion even at very low ϵ^* . It appears that high local density further increases the alignment lifetime of flocks by decreasing rotation of

gliding filaments.

The active isotropic–flocking phase transition can also be crossed by increasing ϵ^* , which increases the number of alignment events, promoting collective motion. However, for flexible filaments (low κ and high ϵ^*), filaments are flexible enough to bend and self-interact via collisions. If filaments collide at approximately a right angle, one or both of the filaments can bend sharply, and form a spiral (Fig. 5C). Spirals are often stable until another collision deforms the filament enough to release it. The system therefore forms a spooling phase when a significant fraction of the filaments in the system are in spools.

The spooling phase in our simulations is related to the frozen, active steady states found in previous experimental work [14]. The principle mechanism of spool formation for driven cytoskeletal filaments has been of significant interest [15, 31, 38–42], with suggestions ranging from defects in the motor lattice to thermal activation. The spools we observe have no preferred direction, because the filaments in our simulations have no preferred curvature. Previous experiments with microtubules and dynein have observed stable filament vortices attributed to filament curvature induced by motors [16], which is absent in our simulations. The spooling phase demonstrated here is governed entirely by spontaneous filament self-interactions and collisions, as found in previous modeling work [31, 40]. Spool formation therefore does not require defects in the protein lattice, pinning of filaments by dead motors, or intrinsic curvature; it can arise solely from steric repulsion and flexibility.

Our phase diagram shows a narrow region of stability for long-range collective motion in the banding and giant flocking phases. While increasing κ always promotes long-range order, increasing ϵ^* too high can effectively break it. At high κ and high ϵ^* , collisions lead to large deformations of flocking and banding filaments, causing buckling. In the simulation shown in Fig. 2C, the filaments repeatedly form a polar band, which buckles and shears, briefly falling apart. The steady state of the system is a dynamic, buckling band that continuously buckles, breaks, and reassembles. Similar dynamic phases have been observed in systems of self-propelled rods [27] and semiflexible filaments driven by motors [32]. Therefore, there seems to exist a Goldilocks range for ϵ^* that facilitates stable, long-range collective motion.

Upon further increasing ϵ^* at high κ , long-range order of flocking filaments decreases to the degree that even metastable polar bands can no longer form, and the system enters the swirling phase. Here, the trajectories of flocking domains have relatively short orientational persistence, because collisions cause large deformation of the flock structure. Occasionally, a sharp bend results in a flock self-interaction, which may form a large, transient vortex of filaments (Fig. 5D). Near the banding–swirling transition, flocking filaments may coalesce into one large flock similar to the polar band phase, but the high degree

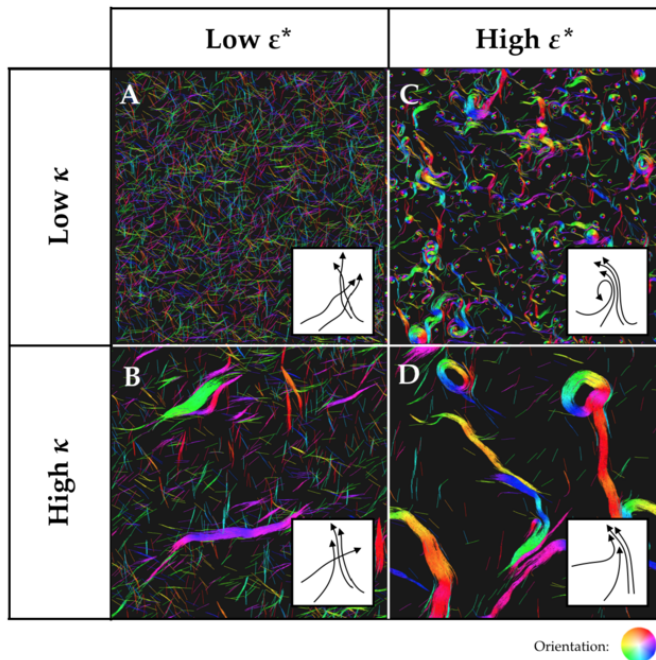


FIG. 5. Diagram depicting the change in collective behavior of active filaments due to varying rigidity κ and interaction energy ϵ^* at a packing fraction of $\phi = 0.2$. Increasing interaction energy decreases the probability of filament crossing, and increases allowed energies of filament collisions. Increasing filament rigidity increases positional and polar order of bundled filaments, and increases resistance to filament bending in collisions. Here, low ϵ^* corresponds to $\epsilon^* = 2.1$, and high $\epsilon^* = 9.3$. Low $\kappa = 20$ and high $\kappa = 100$.

of bending results in shorter end-to-end flock lengths, inhibiting the ability to form stable polar bands.

Our simulations do not display symmetry breaking of the system chirality as observed in some previous work [14, 16, 20], due to zero preferred filament curvature in our model. When an intrinsic curvature is added to filaments with simulation parameters that otherwise form stable polar bands, we observe a rotation in the polar order vector [33], similar to previous simulations of gliding filaments with intrinsic curvature [20]. Future work will likely explore the additional phases arising from chiral symmetry breaking due to intrinsic filament curvature.

The phase diagram presented here makes predictions for the phase behavior of filament gliding experiments over a range of filament persistence length and interaction strength. This could guide future experiments seeking to observe collective behavior. In particular, our model predicts that systems with tunable filament repulsion and rigidity, perhaps mediated by crowding agents or crosslinking proteins, can exhibit a variety of active steady-state behaviors and transport. The ability to control the transition between these behaviors may have applications for drugs targeting cortical cytoskeletal filaments or nanodevices that use cytoskeletal filaments as

molecular shuttles [43, 44]. In addition, our results offer insights into the conditions for filament spool formation.

We would like to thank Michael Stefferson for helpful discussions. This work was funded by the Soft Materials Research Center under NSF MRSEC Grant No. DMR-1420736, and the National Science Foundation under NSF GRFP Award No. DGE 1144083 and NSF Grant No. DMR-1725065. This work utilized the RMACC Summit supercomputer, which is supported by the National Science Foundation (awards ACI-1532235 and ACI-1532236), the University of Colorado Boulder, and Colorado State University. The Summit supercomputer is a joint effort of the University of Colorado Boulder and Colorado State University.

-
- [1] T. Vicsek and A. Zafeiris, *Physics Reports Collective Motion*, **517**, 71 (2012).
 - [2] A. Czirók, E. Ben-Jacob, I. Cohen, and T. Vicsek, *Physical Review E* **54**, 1791 (1996).
 - [3] C. Dombrowski, L. Cisneros, S. Chatkaew, R. E. Goldstein, and J. O. Kessler, *Physical Review Letters* **93**, 098103 (2004).
 - [4] J. K. Parrish, S. V. Viscido, and D. Grünbaum, *The Biological Bulletin* **202**, 296 (2002).
 - [5] I. L. Bajec and F. H. Heppner, *Animal Behaviour* **78**, 777 (2009).
 - [6] J. L. Silverberg, M. Bierbaum, J. P. Sethna, and I. Cohen, *Physical Review Letters* **110**, 228701 (2013).
 - [7] A. A. Hyman and E. Karsenti, *Cell* **84**, 401 (1996).
 - [8] F. J. Nédélec, T. Surrey, A. C. Maggs, and S. Leibler, *Nature* **389**, 305 (1997).
 - [9] T. Surrey, F. Nédélec, S. Leibler, and E. Karsenti, *Science* **292**, 1167 (2001).
 - [10] T. Sanchez, D. T. N. Chen, S. J. DeCamp, M. Heymann, and Z. Dogic, *Nature* **491**, 431 (2012).
 - [11] L. M. Lemma, S. J. DeCamp, Z. You, L. Giomi, and Z. Dogic, *Soft Matter* **15**, 3264 (2019).
 - [12] T. Butt, T. Mufti, A. Humayun, P. B. Rosenthal, S. Khan, S. Khan, and J. E. Molloy, *Journal of Biological Chemistry* **285**, 4964 (2010).
 - [13] V. Schaller, C. Weber, C. Semmrich, E. Frey, and A. R. Bausch, *Nature* **467**, 73 (2010).
 - [14] V. Schaller, C. A. Weber, B. Hammerich, E. Frey, and A. R. Bausch, *Proceedings of the National Academy of Sciences* **108**, 19183 (2011).
 - [15] L. Liu, E. Tüzel, and J. L. Ross, *Journal of Physics: Condensed Matter* **23**, 374104 (2011).
 - [16] Y. Sumino, K. H. Nagai, Y. Shitaka, D. Tanaka, K. Yoshikawa, H. Chaté, and K. Oiwa, *Nature* **483**, 448 (2012).
 - [17] L. Huber, R. Suzuki, T. Krüger, E. Frey, and A. R. Bausch, *Science* **361**, 255 (2018).
 - [18] D. Inoue, B. Mahmot, A. M. Rashedul Kabir, T. Ishrat Farhana, K. Tokuraku, K. Sada, A. Konagaya, and A. Kakugo, *Nanoscale* **7**, 18054 (2015).
 - [19] A. Saito, T. Ishrat Farhana, A. M. Rashedul Kabir, D. Inoue, A. Konagaya, K. Sada, and A. Kakugo, *RSC Advances* **7**, 13191 (2017).

- [20] K. Kim, N. Yoshinaga, S. Bhattacharyya, H. Nakazawa, M. Umetsu, and W. Teizer, *Soft Matter* **14**, 3221 (2018).
- [21] T. Vicsek, A. Czirók, E. Ben-Jacob, I. Cohen, and O. Shochet, *Physical Review Letters* **75**, 1226 (1995).
- [22] H. Levine, W.-J. Rappel, and I. Cohen, *Physical Review E* **63**, 017101 (2000).
- [23] G. Grégoire and H. Chaté, *Physical Review Letters* **92**, 025702 (2004).
- [24] M. Aldana, V. Dossetti, C. Huepe, V. M. Kenkre, and H. Larralde, *Physical Review Letters* **98**, 095702 (2007).
- [25] H. Chaté, F. Ginelli, G. Grégoire, and F. Raynaud, *Physical Review E* **77**, 046113 (2008).
- [26] P. Kraikivski, R. Lipowsky, and J. Kierfeld, *Physical Review Letters* **96**, 258103 (2006).
- [27] F. Ginelli, F. Peruani, M. Bär, and H. Chaté, *Physical Review Letters* **104**, 184502 (2010).
- [28] F. Peruani, J. Starruß, V. Jakovljevic, L. Søgaaard-Andersen, A. Deutsch, and M. Bär, *Physical Review Letters* **108**, 098102 (2012).
- [29] M. Abkenar, K. Marx, T. Auth, and G. Gompper, *Physical Review E* **88**, 062314 (2013).
- [30] H.-S. Kuan, R. Blackwell, L. E. Hough, M. A. Glaser, and M. D. Betterton, *Physical Review E* **92** (2015).
- [31] Ö. Duman, R. E. Isele-Holder, J. Elgeti, and G. Gompper, *Soft Matter* **14**, 4483 (2018).
- [32] G. Vliegenthart, A. Ravichandran, M. Ripoll, T. Auth, and G. Gompper, *arXiv:1902.07904 [cond-mat]* (2019).
- [33] See Supplemental Material at [URL] for computational model details and methodology, equations for order parameters, quantification of phase behavior, and discussions about filament orientation autocorrelation and alignment probabilities.
- [34] T. Gao, R. Blackwell, M. A. Glaser, M. D. Betterton, and M. J. Shelley, *Physical Review Letters* **114**, 048101 (2015).
- [35] J. M. Moore, “Simcore v0.1.2,” <http://github.com/jeffmm/simcore.git> (2019).
- [36] M. Doi and S. F. Edwards, *The Theory of Polymer Dynamics* (Clarendon Press, 1988).
- [37] A. Montesi, D. C. Morse, and M. Pasquali, *The Journal of Chemical Physics* **122**, 084903 (2005).
- [38] I. Luria, J. Crenshaw, M. Downs, A. Agarwal, S. Banavara Seshadri, J. Gonzales, O. Idan, J. Kamcev, P. Katira, S. Pandey, T. Nitta, S. R. Phillpot, and H. Hess, *Soft Matter* **7**, 3108 (2011).
- [39] A. T. Lam, C. Curschellas, D. Krovvidi, and H. Hess, *Soft Matter* **10**, 8731 (2014).
- [40] R. E. Isele-Holder, J. Elgeti, and G. Gompper, *Soft Matter* **11**, 7181 (2015).
- [41] V. VanDelinder, S. Brener, and G. D. Bachand, *Biomacromolecules* **17**, 1048 (2016).
- [42] Z. Mokhtari and A. Zippelius, *Physical Review Letters* **123**, 028001 (2019).
- [43] T. Nitta, A. Tanahashi, M. Hirano, and H. Hess, *Lab on a Chip* **6**, 881 (2006).
- [44] H. Hess, *Annual Review of Biomedical Engineering* **13**, 429 (2011).

Supplemental Material: Collective motion of driven semiflexible filaments tuned by soft repulsion and stiffness

Jeffrey M. Moore,¹ Tyler N. Thompson,¹ Matthew A. Glaser,¹ and Meredith D. Betterton^{1,2}

¹*Department of Physics, University of Colorado, Boulder, CO 80309*

²*Department of Molecular, Cellular, and Developmental Biology, University of Colorado, Boulder, CO 80309*

(Dated: March 26, 2022)

I. SIMULATION MODEL

For the representation of semiflexible filaments, we adopt the algorithm for a bead-rod model of a wormlike chain of Pasquali et al. [1]. Filaments are represented by N sites (beads) and $N - 1$ segments (rods), with fixed segment length a , total contour length $L = (N - 1)a$, and total anisotropic friction, $\zeta_{\perp}^{\text{tot}} = 2\zeta_{\parallel}^{\text{tot}}$. The position of each site \mathbf{r}_i is updated using a midstep algorithm

$$\begin{aligned}\mathbf{r}_i^{(1/2)} &= \mathbf{r}_i^{(0)} + \frac{\Delta t}{2} \mathbf{v}_i^{(0)}, \\ \mathbf{r}_i^{(1)} &= \mathbf{r}_i^{(0)} + \Delta t \mathbf{v}_i^{(1/2)},\end{aligned}\tag{1}$$

where Δt is the time step, $\mathbf{v}_i^{(0)}$ is the initial velocity of site i at initial position $\mathbf{r}_i^{(0)}$, and $\mathbf{v}_i^{(1/2)}$ is the velocity of site i recalculated at the midstep position $\mathbf{r}_i^{(1/2)}$, but using the same nondeterministic forces as in $\mathbf{v}_i^{(0)}$. Each site i is assigned an orientation, corresponding to the orientation of the segment attaching it to site $i + 1$,

$$\mathbf{u}_i = \frac{\mathbf{r}_{i+1} - \mathbf{r}_i}{|\mathbf{r}_{i+1} - \mathbf{r}_i|} = \frac{1}{a}(\mathbf{r}_{i+1} - \mathbf{r}_i).\tag{2}$$

The orientation of the last site of the filament is set equal to that of its only neighboring segment, so that $\mathbf{u}_N = \mathbf{u}_{N-1}$. The velocity of each site is

$$\mathbf{v}_i = \mathbf{H}_{ij} \cdot \mathbf{F}_j^{\text{tot}},\tag{3}$$

where \mathbf{H}_{ij} is an anisotropic mobility tensor, and is the mobility of site i in response to a force on site j . The total force on site i is the sum

$$\mathbf{F}_i^{\text{tot}} = \mathbf{F}_i^{\text{bend}} + \mathbf{F}_i^{\text{metric}} + \mathbf{F}_i^{\text{tension}} + \mathbf{F}_i^{\text{ext}} + \boldsymbol{\eta}_i,\tag{4}$$

which include both deterministic and nondeterministic forces. Deterministic forces include filament bending forces, metric forces, tension forces, and external forces. Nondeterministic forces include geometrically-projected random forces $\boldsymbol{\eta}_i$, which are described in detail by Montesi et al. [1].

The mobility tensor can be written as an inverse site friction tensor

$$\begin{aligned}\mathbf{H}_{ij} &= \delta_{ij} \zeta_j^{-1}, \\ \zeta_i^{-1} &= \frac{1}{\zeta_{\parallel}^i} \tilde{\mathbf{u}}_i \otimes \tilde{\mathbf{u}}_i + \frac{1}{\zeta_{\perp}^i} (\mathbf{I} - \tilde{\mathbf{u}}_i \otimes \tilde{\mathbf{u}}_i).\end{aligned}\tag{5}$$

where $\tilde{\mathbf{u}}_i$ is a vector tangent to site i , the \otimes symbol denotes the outer product, and the parallel and perpendicular friction coefficients corresponding to site i are ζ_{\parallel}^i and ζ_{\perp}^i respectively. The tangent vector is the average of the orientations \mathbf{u}_i of its neighboring segments,

$$\tilde{\mathbf{u}}_i = \frac{(\mathbf{u}_i + \mathbf{u}_{i-1})}{|\mathbf{u}_i + \mathbf{u}_{i-1}|}\tag{6}$$

for $2 \leq i \leq N$, and $\tilde{\mathbf{u}}_1 = \mathbf{u}_1$, $\tilde{\mathbf{u}}_N = \mathbf{u}_{N-1}$ at the chain ends. The position update routine in Eqn. 1 can be rewritten in terms of the inverse site friction tensor as

$$\mathbf{r}_i^{(1/2)} = \mathbf{r}_i^{(0)} + \frac{\Delta t}{2} \zeta_i^{-1, (0)} \cdot \mathbf{F}_i^{\text{tot}, (0)}, \quad (7)$$

$$\mathbf{r}_i^{(1)} = \mathbf{r}_i^{(0)} + \Delta t \zeta_i^{-1, (1/2)} \cdot \mathbf{F}_i^{\text{tot}, (1/2)}, \quad (8)$$

The diffusion of the wormlike chain is $D = k_B T / \zeta = k_B T / N \zeta^i$, where ζ^i is the local friction due to each site, which depends on the aspect ratio L/d where d is the diameter of the chain. In the regime of rigid, infinitely thin rods, the total coefficient of friction is given by [2],

$$\lim_{L/d \rightarrow \infty} \zeta_{\perp}^{\text{tot}} = 4\pi\eta_s L\epsilon. \quad (9)$$

where $\epsilon = 1/\ln(L/d)$. In the finite aspect ratio case, this friction coefficient is multiplied by a geometric factor

$$f(\epsilon) = \frac{1 + 0.64\epsilon}{1 - 1.15\epsilon} + 1.659\epsilon^2. \quad (10)$$

Therefore, each site experiences a local friction given by

$$\zeta_{\perp}^i = 4\pi\eta_s a \epsilon f(\epsilon). \quad (11)$$

The bending energy of a discrete wormlike chain for $N \gg 1$ is approximated by

$$U = -\frac{\psi}{a} \sum_{k=2}^{N-1} \mathbf{u}_k \cdot \mathbf{u}_{k-1}, \quad (12)$$

where ψ is the bending rigidity, which is related to the persistence length L_p of the wormlike chain as $\psi/k_B T = L_p$. The bending force is then $\mathbf{F}_i^{\text{bend}} = -\partial U / \partial \mathbf{r}_i$. The implementation of the bending forces coincides with metric forces, which come from a metric pseudo-potential

$$U_{\text{metric}} = \frac{k_B T}{2} \ln(\det \hat{\mathbf{G}}), \quad (13)$$

and $\hat{\mathbf{G}}$ is the metric tensor, which is an $(N-1) \times (N-1)$ tridiagonal matrix. $\hat{\mathbf{G}}$ has diagonal terms $d_i = 2$ and the off-diagonal terms depend on the cosine of the angle between neighboring segments, $c_i = -\mathbf{u}_i \cdot \mathbf{u}_{i-1}$. The metric pseudo-potential is necessary for the filament conformation to have the expected statistical behavior in the flexible limit, $L_p \ll L$.

It was shown by Pasquali and Morse [3] that the bending forces and metric forces could be calculated together as one force term,

$$\mathbf{F}_i^{\text{bend}} + \mathbf{F}_i^{\text{metric}} = \frac{1}{a} \sum_{k=2}^{N-1} \psi_k^{\text{eff}} \frac{\partial(\mathbf{u}_k \cdot \mathbf{u}_{k-1})}{\partial \mathbf{r}_i}, \quad (14)$$

where ψ^{eff} replaces the true bending rigidity ψ as an effective rigidity with a conformational dependence,

$$\psi_i^{\text{eff}} = \psi + k_B T a \hat{G}_{i-1,i}^{-1}. \quad (15)$$

The derivative in the equation for the combined forces can be evaluated from

$$\frac{\partial \mathbf{u}_k}{\partial \mathbf{r}_i} = \frac{1}{a} (\delta_{i,k+1} - \delta_{i,k}) (\mathbf{I} - \mathbf{u}_k \otimes \mathbf{u}_k), \quad (16)$$

so the two forces can be written

$$\mathbf{F}_i^{\text{bend}} + \mathbf{F}_i^{\text{metric}} = \frac{1}{a^2} \sum_{k=2}^{N-1} \psi_k^{\text{eff}} \left((\delta_{i,k+1} - \delta_{i,k}) (\mathbf{I} - \mathbf{u}_k \otimes \mathbf{u}_k) \mathbf{u}_{k-1} + (\delta_{i,k} - \delta_{i,k-1}) (\mathbf{I} - \mathbf{u}_{k-1} \otimes \mathbf{u}_{k-1}) \mathbf{u}_k \right). \quad (17)$$

For an inextensible wormlike chain, the positions of N sites must satisfy $N - 1$ constraints C_μ where

$$C_\mu = |\mathbf{r}_{\mu+1} - \mathbf{r}_\mu| = a, \quad (18)$$

for $\mu = 1, \dots, N - 1$. Differentiating the constraints with respect to the site positions \mathbf{r}_i yields a vector

$$\mathbf{n}_{i\mu} = \mathbf{u}_\mu (\delta_{i,\mu+1} - \delta_{i,\mu}). \quad (19)$$

The geometrically projected random forces $\boldsymbol{\eta}_i$ must satisfy the property

$$\boldsymbol{\eta}_i \cdot \mathbf{n}_{i\mu} = 0, \quad (20)$$

so that the $3N$ dimensional vector of random forces $\boldsymbol{\eta}_i$ is locally tangent to the $3N - (N - 1) = 2N + 1$ dimensional hypersurface to which the system is confined.

The geometrically projected random forces $\boldsymbol{\eta}$ are calculated from

$$\begin{aligned} \boldsymbol{\eta}_i &= \boldsymbol{\eta}'_i - \mathbf{n}_{i\mu} \hat{\eta}_\mu, \\ &= \boldsymbol{\eta}'_i + \hat{\eta}_i \mathbf{u}_i - \hat{\eta}_{i-1} \mathbf{u}_{i-1}, \end{aligned} \quad (21)$$

where $\boldsymbol{\eta}'_i$ are the unprojected random forces and $\hat{\eta}_\mu$ is the component of the $3N$ dimensional unprojected random force vector along direction $\mathbf{n}_{i\mu}$. The unprojected random forces at each timestep are

$$\begin{aligned} \boldsymbol{\eta}'_i &= \sqrt{24k_B T / \Delta t} \boldsymbol{\zeta}_i^{1/2} \cdot \boldsymbol{\xi}_i \\ &= \sqrt{24k_B T / \Delta t} \left(\boldsymbol{\zeta}_\perp^{1/2} \boldsymbol{\xi}_i + (\boldsymbol{\zeta}_\parallel^{1/2} - \boldsymbol{\zeta}_\perp^{1/2}) \tilde{\mathbf{u}}_i \otimes \tilde{\mathbf{u}}_i \cdot \boldsymbol{\xi}_i \right), \end{aligned} \quad (22)$$

where $\boldsymbol{\xi}_i$ is a spatial vector whose elements are uniformly distributed random numbers between $-0.5, 0.5$ [1, 4].

To calculate $\hat{\eta}_i$, we solve the set of $N - 1$ linear equations

$$\sum_{\nu=1}^{N-1} \hat{G}_{\mu\nu} \hat{\eta}_\nu = (\boldsymbol{\eta}'_{\mu+1} - \boldsymbol{\eta}'_\mu) \cdot \mathbf{u}_\mu = p_\mu, \quad (23)$$

where $\hat{\mathbf{G}}$ is the metric tensor. In matrix notation, this is equivalent to solving $\hat{\mathbf{G}}\hat{\boldsymbol{\eta}} = \mathbf{p}$ for $\hat{\boldsymbol{\eta}}$, and can be solved in $\mathcal{O}(N)$ steps using LU decomposition for tridiagonal matrices. Once the system is solved for $\hat{\eta}_i$, we use Eqn. 21 to solve for the geometrically projected random forces. While the deterministic forces are recalculated and applied at each half step of the simulation, the geometrically projected random forces are only calculated once per full simulation step at the initial site positions $\mathbf{r}_i^{(0)}$, and applied at each half step of the algorithm.

To calculate the tension \mathcal{T}_i , we require that the system constraints are constant, i.e. $\dot{C}_\mu = 0$. This is equivalent to solving the system of linear equations

$$\sum_{\nu=1}^{N-1} \hat{H}_{\mu\nu} \mathcal{T}_\nu = \mathbf{u}_\mu \cdot (\boldsymbol{\zeta}_{\mu+1}^{-1} \cdot \mathbf{F}_{\mu+1}^{\text{uc}} - \boldsymbol{\zeta}_\mu^{-1} \cdot \mathbf{F}_\mu^{\text{uc}}) = q_\mu, \quad (24)$$

where $\mu = 1, \dots, N - 1$. In matrix notation, this can be written as $\hat{\mathbf{H}}\boldsymbol{\mathcal{T}} = \mathbf{q}$, where $\hat{\mathbf{H}}$ is another tridiagonal $(N - 1) \times (N - 1)$ matrix

$$\hat{H}_{\mu\nu} = \sum_{i=1}^N \mathbf{n}_{i\mu} \cdot \boldsymbol{\zeta}_i^{-1} \cdot \mathbf{n}_{i\nu} \quad (25)$$

or

$$\hat{\mathbf{H}} = \begin{bmatrix} b_1 & a_2 & 0 & \dots & 0 & 0 \\ a_2 & b_2 & a_3 & 0 & \dots & 0 \\ 0 & a_3 & b_3 & a_4 & 0 & \dots \\ \dots & \dots & \dots & \dots & \dots & \dots \\ \dots & 0 & a_{N-3} & b_{N-3} & a_{N-2} & 0 \\ 0 & \dots & 0 & a_{N-2} & b_{N-2} & a_{N-1} \\ 0 & 0 & \dots & 0 & a_{N-1} & b_{N-1} \end{bmatrix}, \quad (26)$$

with diagonal and off-diagonal elements

$$\begin{aligned} b_\mu &= \frac{2}{\zeta_\perp} + \left(\frac{1}{\zeta_\parallel} - \frac{1}{\zeta_\perp} \right) \left((\tilde{\mathbf{u}}_\mu \cdot \mathbf{u}_\mu)^2 + (\tilde{\mathbf{u}}_{\mu+1} \cdot \mathbf{u}_\mu)^2 \right), \\ a_\mu &= -\frac{1}{\zeta_\perp} \mathbf{u}_{\mu+1} \cdot \mathbf{u}_\mu - \left(\frac{1}{\zeta_\parallel} - \frac{1}{\zeta_\perp} \right) \left((\tilde{\mathbf{u}}_\mu \cdot \mathbf{u}_{\mu+1})(\tilde{\mathbf{u}}_\mu \cdot \mathbf{u}_\mu) \right). \end{aligned} \quad (27)$$

and can be solved in a similar manner as Eqn. 23. The tension forces are then

$$\mathbf{F}_i^{\text{tension}} = \mathcal{T}_i \mathbf{u}_i - \mathcal{T}_{i-1} \mathbf{u}_{i-1}. \quad (28)$$

External forces $\mathbf{F}_i^{\text{ext}}$ include forces from filament-filament interactions and self-propulsion forces from the driving of molecular motors. The filament-filament interaction forces are calculated from the derivative of the general exponential model potential (GEM-8)

$$U(r) = \begin{cases} \epsilon e^{-(r/\sigma)^8} & \text{if } r < \sqrt{2}\sigma, \\ 0 & \text{otherwise.} \end{cases} \quad (29)$$

where r is the minimum distance between neighboring filament segments and σ is the unit length used in the simulation, defined to be the diameter of a filament.

Forces from molecular motors are modeled in our simulations as a uniform force density f_{dr} that is directed along the local filament segment orientations,

$$\mathbf{F}_{\text{dr}} = f_{\text{dr}} \mathbf{u}_i. \quad (30)$$

The assumptions of this model are that lattice defects are negligible for observing collective behavior of gliding filaments, and that motor binding and unbinding events occur at fast enough rates such that their behavior need not be explicitly included in the model. These assumptions are guided by experimental observations that filament velocities are constant in gliding assays, despite the presence of filament crossing events that certainly require a large number of unbinding and binding events [5].

II. MODEL IMPLEMENTATION

Simulation software for the filament model is written in C++ and is publicly available online [6]. The simulations were run on the Summit computing cluster [7] and parallelized using OpenMP on 24 CPUs.

III. MODEL VALIDATION

We tested the model to ensure agreement with theory for Brownian wormlike chains. Filament diffusion was validated by measuring the mean-squared displacement (MSD) and vector correlation function (VCF) for filaments in the rigid regime ($L_p \gg L$) and matching the expected values for slender, rigid filaments [2] (Fig. 1).

Filament bending was validated by ensuring that the conformations sampled by a filament at thermal equilibrium matched the expected statistical behavior. The distribution of angles between joining filament segments should be a Boltzmann distribution $P(\cos \theta) \propto e^{L_p/L \cos \theta}$. Following Pasquali et al. [1], we fit a histogram of filament angles from our simulation and found good agreement with the theoretical distribution (Fig. 2).

We also validated the bending model by quantifying the filament buckling behavior for rigid filaments that were placed under a load. For a rigid filament with a persistence length L_p , we expect the maximum load that an unconstrained filament can withstand before buckling to be given by Euler's critical load for a column, $F_{cr} = \frac{\pi^2 L_p k_B T}{L^2}$. To measure the critical load, we linearly increased a Hookean spring force between filament ends and recorded the force at the time when the end-to-end distance of the filament sharply deviated from the filament contour length. Varying both contour length and persistence length, we compared our measured values of the critical load to theory and found good agreement with the expected values (Fig. 3).

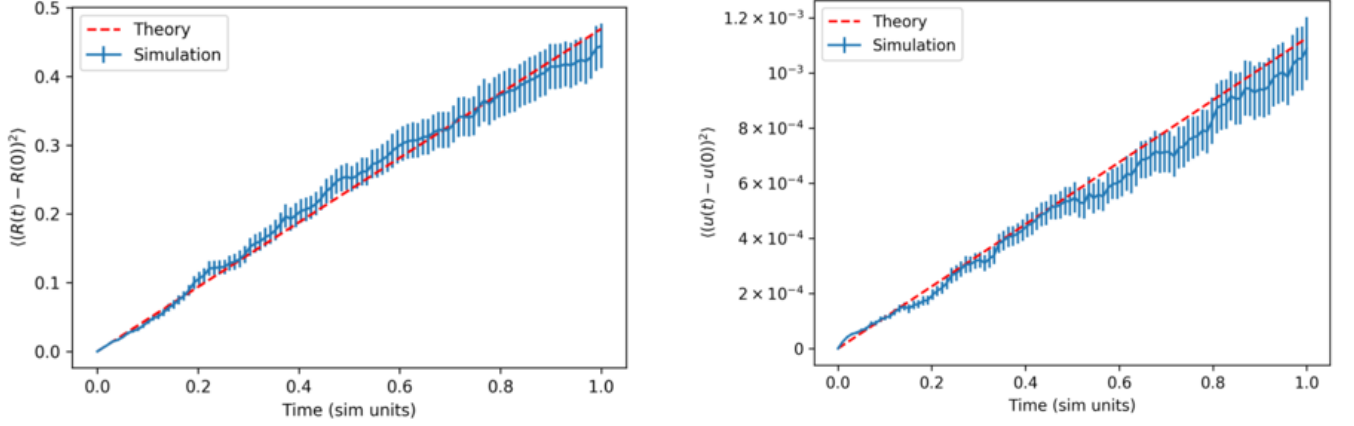


FIG. 1. Left, simulation and theoretical comparison of the mean-squared displacement (MSD) averaged over 100 rigid filaments ($L_p/L = 1000$). The expected value of the MSD for a rigid filament of length L and diameter σ is given by $\langle (\mathbf{R}(t) - \mathbf{R}(0))^2 \rangle = 6D_{tr}t$, where \mathbf{R} is the center of mass of the filament and D_{tr} is the translational diffusion coefficient $D_{tr} = \frac{\ln(L/\sigma)}{3\pi\eta L} k_B T$, where η is the fluid viscosity. Right, simulation and theoretical comparison of the vector correlation function (VCF) averaged over 100 rigid filaments ($L_p/L = 1000$). The time axis is in simulation units τ , where τ is the average time for a sphere of diameter σ to diffuse its own diameter. The expected value of the VCF for a rigid filament of length L and diameter σ is given by $\langle (\mathbf{u}(t) - \mathbf{u}(0))^2 \rangle = 2(1 - \exp(-2D_r t))$, where \mathbf{u} is the orientation of the filament and D_r is the rotational diffusion coefficient $D_r = \frac{3\ln(L/\sigma)}{\pi\eta L^3} k_B T$. The time axes are in simulation units τ , where τ is the average time for a sphere of diameter σ to diffuse its own diameter.

IV. SIMULATION PARAMETERS

Key parameters of our simulation include the filament length L , diameter σ , persistence length L_p , driving force per unit length f_{dr} , repulsive energy ϵ , simulation box diameter L_{sys} , and filament density. In our simulations, all filaments have an aspect ratio $l = L/\sigma = 60$, and the system size is $l_{sys} = L_{sys}/L = 20$. In our dimensionless reduced units, σ , $k_B T$, and D are set to unity, where D is the diffusion coefficient of a sphere with diameter σ . The driving force in reduced units is $f_{dr} = 30$, so that the Péclet number is $Pe = f_{dr} L^2 / k_B T \approx 10^5$. When the repulsive energy ϵ in the GEM-8 potential has a value $\epsilon_{dr} = 8.6$ in reduced units, the repulsive interaction between particles has a maximum force of 30, equal to the force applied by driving a particle of diameter σ . The repulsion parameter ϵ^* is then rescaled by ϵ_{dr} so that $\epsilon^* = l = 60$ corresponds to fully impenetrable filaments for our choice of Péclet number.

The dimensionless parameters of interest when exploring the phase behavior of collective semiflexible filaments are $\kappa = L_p/L$, the rescaled energy $\epsilon^* = \epsilon/\epsilon_{dr}$, and packing fraction $\phi = A_{fil}/A_{sys}$, where A_{sys} is the area of the simulation box and $A_{fil} = N(L\sigma + \pi\sigma^2)$ is the total area occupied by N spherocylindrical filaments. The timestep used in our half step integration algorithm was $\Delta t = 10^{-4}\tau$, where τ is the average time for a sphere of diameter σ to diffuse its own diameter.

Filaments in the simulation were initialized by randomly inserting filaments parallel to one axis of the simulation box in a nematic arrangement, and allowing the filaments to diffuse for 100τ steps before driving the filaments. Simulations terminated once they were determined to have reached a steady state, when order parameters appeared to converge to constant values.

V. ORDER PARAMETERS

Six order parameters quantify the system phase behavior, including global polar order P , global nematic order Q , contact number c , local polar order p , structural order S , and spiral number s .

The global polar order P is the magnitude of the steady-state average orientation vector,

$$P = |\mathbf{P}| = \frac{1}{Nn} \sum_{i=1}^{Nn} \mathbf{u}_i, \quad (31)$$

where \mathbf{u}_i is the orientation of the i^{th} filament segment for N filaments each composed of n segments. The nematic

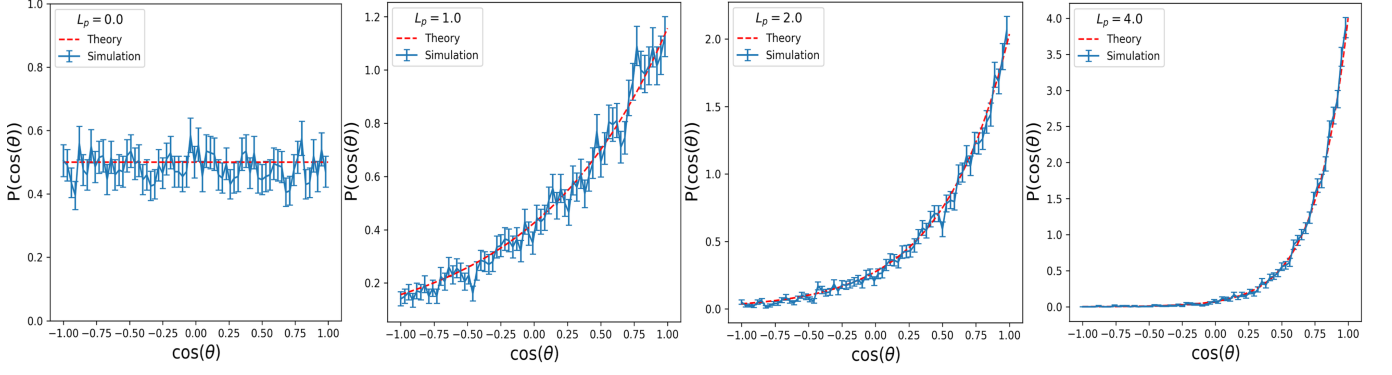


FIG. 2. Simulation and theoretical comparison of the distributions of angles between segments for filaments with $L_p = 0, 1, 4$, and 8 . Simulations were carried out by averaging the results for 100 non-interacting filaments of length $L = 20\sigma$ and segment length $a = \sigma$ diffusing for $10^4\tau$.

order is the maximum eigenvalue Q of the 2D nematic order tensor

$$\mathbf{Q} = \frac{1}{Nn} \sum_{i=1}^{Nn} (2\mathbf{u}_i \otimes \mathbf{u}_j - \mathbf{I}), \quad (32)$$

where \mathbf{I} is the unit tensor. The contact number is a measure of filament crowding, given by the system average of the segment contact number,

$$c_i = \sum_{\substack{j \neq i \\ \text{inter}}}^{Nn} e^{-\sigma s_{ij}^2}, \quad (33)$$

where s_{ij} is the minimum distance between segments, with the sum excluding all intrafilament segments. The local polar order parameter is the system average of the local polar order of filament segments,

$$p_i = \frac{\sum_{\substack{j \neq i \\ \text{inter}}}^{Nn} \mathbf{u}_i \cdot \mathbf{u}_j e^{-\sigma s_{ij}^2}}{c_i}, \quad (34)$$

where the sum again excludes intrafilament segments.

The positional order parameter $S(q_0)$ is derived from the structure factor, which is the Fourier transform of center-of-mass positions of filament segments

$$S(\mathbf{q}) = \frac{1}{N} \sum_{\substack{k \neq j \\ \text{inter}}}^N n e^{i\mathbf{q} \cdot (\mathbf{R}_k - \mathbf{R}_j)}, \quad (35)$$

where \mathbf{R}_j is the center-of-mass position of the j_{th} filament segment, and the sum excludes segments belonging to the same filament. The structure factor is then radially averaged, and a derivative filter is used to find the intensity at the first radial wavenumber $q_0 \neq 0$ where the radially-averaged structure factor is locally maximal, $S(q_0)$ (Fig. 4). The positional order parameter is defined as $\log_{10} S(q_0)$. A high positional order reflects a well-ordered filament structure, and a low positional order indicates a disordered state, such as the active isotropic phase.

The spiral number is a measure of average filament shape,

$$s = \frac{1}{2\pi} \sum_i^N \theta_i, \quad (36)$$

where θ_i is the angle swept by traversing the tail-to-head contour of filament i . A straight filament has $s = 0$ and a filament bent into a perfect circle has $s = 1$.

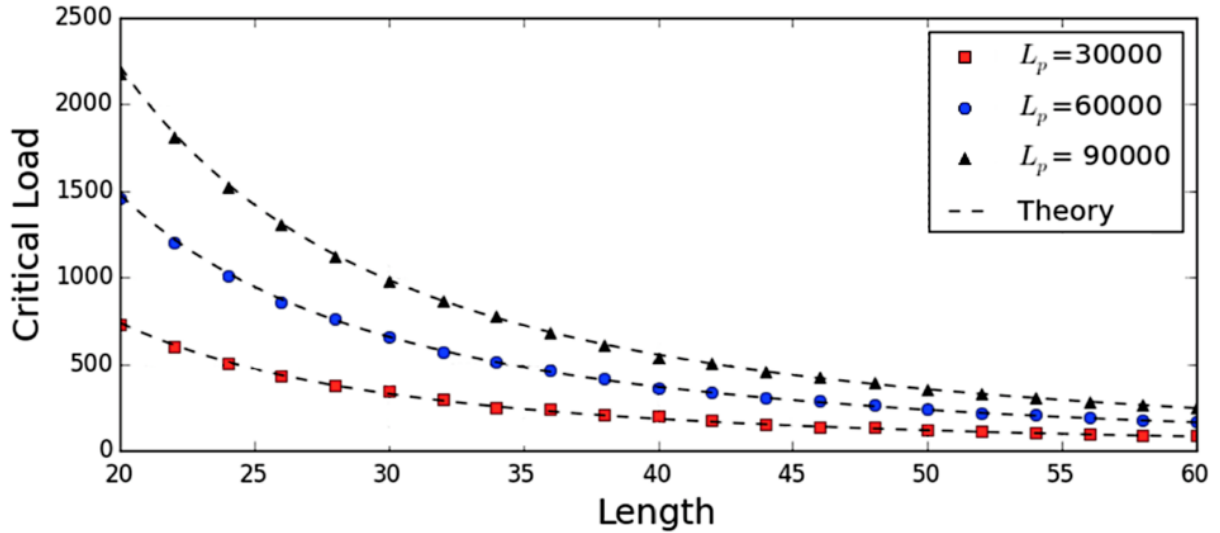


FIG. 3. Simulation and theoretical comparison of the critical buckling load for filaments with varying length and persistence length to ensure agreement with Euler's formula for a buckling column. The critical load is given in simulation units, $k_B T / \sigma$.

VI. COLLECTIVE FILAMENT PHASE BEHAVIOR

We use the order parameters to quantify the phase behaviors observed in our simulations, and find six distinct phases: active isotropic, flocking, banding, swirling, and spooling. We constructed a phase diagram in a 3D parameter space with varying κ , ϵ^* , and ϕ . At each density, we used a support vector machine algorithm [8] to draw the 2D phase boundaries with respect to κ and ϵ^* using a radial basis function kernel $\mathcal{K}(x - x') = \alpha \exp(-|x - x'|/2\sigma^2)$. The hyperparameters used to make the phase diagram were $\alpha = 60$ and $\sigma = 5$, chosen for boundary smoothness. Coexistence regions were added based on observations of the simulation steady state.

In the active isotropic phase, low filament repulsion prevents alignment of colliding filaments (Fig. 5). As a result, filaments are isotropically oriented and the system is typically disordered (see Table I for typical order parameter values).

When repulsion and persistence length are increased, the probability of filament alignment between two interacting filaments increases and the active isotropic phase can transition to the flocking phase (Fig. 6). In the flocking phase, collective motion begins to emerge as filaments coalesce into local polar domains. Flocks are dynamic with filaments continuously joining and leaving, and flocks frequently merge and divide. In the flocking phase, the global polar and nematic order are low, while the contact number, local polar order, and positional order are moderate to high.

In the banding phase, all flocks in the system coalesce into polar domains that span the length of the system (Fig. 7). At moderate filament densities ($\phi = 0.1, 0.2$), one persistent polar band forms, leading to high global polar order P . At high density ($\phi = 0.4$), multiple bands form parallel to the axis of filament insertion with random polarity determined by initial conditions, and may have high local polar order p and a global polar order P determined by the number of antiparallel bands (Fig. 8). Distinct from both banding and flocking is the giant flock phase that appears at low filament density ($\phi = 0.04$), where all flocks coalesce into one persistent and stable domain (Fig. 9). However the characteristic length of the domain does not span the length scale of the system, and is unable to form a band. The giant flock therefore has high global polar order, with a polar order vector that rotates randomly over time. Each of these phases have high positional order, local polar order, and contact number.

At high rigidity and repulsion, filaments enter the swirling phase, which is characterized by large, polar flocks, but with trajectories that have relatively low directional persistence (Fig. 11). The collisions in this phase cause large deformations of flocks, occasionally resulting in a flock self-interaction, which may form large, metastable vortices of filaments. The swirling phase is characterized by large local polar order and positional order, low global polar order, and moderate spiral number and contact number.

When filaments are flexible and repulsion is large, filaments can enter the spooling phase (Fig. 10). In the spooling phase, a filament can bend far enough to self-interact, allowing the possibility of trapping itself into a shape that resembles a spiral. When a large number of filaments in the system condense into spirals, the average spiral number becomes large, and the system has high local polar order and positional order.

We used the order parameters to assign each simulation a six-dimensional vector in order-parameter space. In order

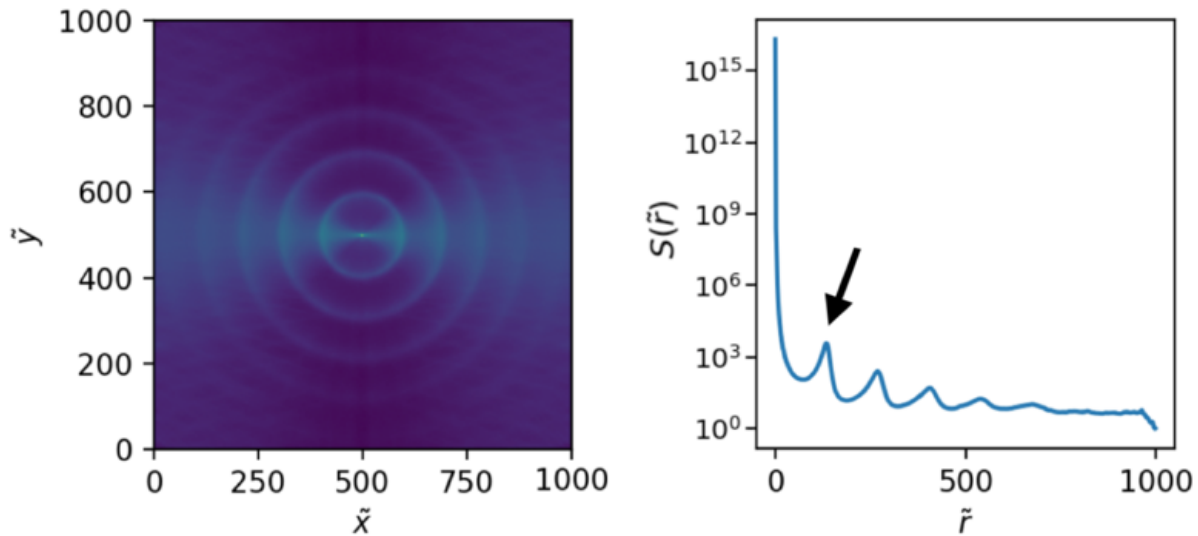


FIG. 4. Left, structure factor in Fourier space. Right, radially-averaged structure factor. The logarithm of S at the first peak at a radial wavenumber greater than 0, indicated by the black arrow, is the positional order parameter.

to visualize how well separated the different phases are with respect to the order parameters, we used a t-distributed Stochastic Neighbor Embedding algorithm [9] to project the simulation coordinates onto a 2D plane. This allows us to visualize how well separated each of the phases are with respect to the order parameters (Fig. 12). While the active isotropic and banding phases are very separated, the spooling, swirling, and flocking phases are slightly intermixed due to phase coexistence near the transition boundaries.

VII. FILAMENT ALIGNMENT PROBABILITY

In order to determine the probability that two intersecting filaments align P_{align} , we simulated the intersection of two filaments in the absence of Brownian noise, sampled from 100 initial collision angles ranging between 0 and 180° . When the minimum angle between filaments is greater than a critical angle θ_c , the intersecting filaments always overlap and cross each other, and below the critical angle the filaments align. The alignment probability is found by assuming a uniform likelihood of initial collision angles between the two intersecting filaments, $2\theta_c/180^\circ$.

The critical angle increases with increasing repulsion, requiring collision angles closer to 90° in order for two filaments to cross each other (Fig. 13). On the other hand, increasing filament rigidity lowers the critical angle, resulting in a lower alignment probability. Despite having a lower alignment probability, increasing filament rigidity increases collective motion of interacting filaments because rigid filaments have trajectories that are more ballistic than those of flexible filaments, resulting in longer alignment lifetimes of aligned filaments.

VIII. FILAMENT ORIENTATION AUTOCORRELATION

The filament orientation autocorrelation was calculated using

$$\phi(t) = \frac{1}{T} \int_0^T \mathbf{u}(t') \cdot \mathbf{u}(t' + t) dt', \quad (37)$$

where $\mathbf{u}(t)$ is the orientation of the filament at time t , and the correlation was averaged over N intervals of duration $T + t$. The result was fit to an exponential function $\langle \phi(t) \rangle = \exp(-t/\tau_\phi)$ to find the characteristic autocorrelation lifetime τ_ϕ .

Filament orientation autocorrelation lifetimes lengthen with increasing filament rigidity κ and shorten with increasing repulsion ϵ^* , due to an increased number of alignment events for intersecting filaments. For a fixed repulsion ϵ^* , a longer orientation autocorrelation lifetime correlates with collective motion, which suggests that the angular persistence of filament trajectories contributes to the formation of persistent flocks and bands. For more ballistic

Phase	Global polar order	Global nematic order	Local polar order	Contact number	Positional order	Spiral number
Active isotropic	$P \approx 0$	$Q \approx 0$	$p < 0.25$	$c < 1$	$\log_{10} S(q_0) < 0.5$	$s \approx 0$
Flocking	$P \approx 0$	$Q \approx 0$	$0.25 < p < 0.75$	$1 < c < 5$	$0.5 < \log_{10} S(q_0) < 1$	$s \approx 0$
Giant flock	$P \approx 1$	$Q \approx 1$	$p > 0.8$	$c > 5$	$\log_{10} S(q_0) > 1$	$s \approx 0$
Polar band	$P \approx 1$	$Q \approx 1$	$p > 0.8$	$c > 5$	$\log_{10} S(q_0) > 1$	$s \approx 0$
Nematic band	$0 < P < 1$	$Q \approx 1$	$p > 0.8$	$c > 5$	$\log_{10} S(q_0) > 1$	$s \approx 0$
Spooling	$P \approx 0$	$Q \approx 0$	$0.25 < p < 0.75$	$c < 1$	$0.5 < \log_{10} S(q_0) < 1$	$s > 0.15$
Swirling	$P \approx 0$	$Q \approx 0$	$p > 0.75$	$1 < c < 5$	$\log_{10} S(q_0) > 1$	$0.05 < s < 0.1$

TABLE I. Typical order parameter values for the dynamic phases observed in simulations.

trajectories, filaments that align can remain aligned for longer time, thus increasing the probability of aligning with more filaments along that trajectory, which may cause the accumulation of aligned filaments to form persistent flocks.

IX. INTRINSIC CURVATURE

An intrinsic curvature $d\phi/ds$ was added to the filament model by adjusting the bending forces \mathbf{F}_{bend} so that they are zero when the angular difference between adjacent segment orientations is $\phi_0 = ad\phi/ds$, where a is the filament segment length. This was achieved by rotating each segment orientation \mathbf{u}_k by half of the angle $-\phi_0$ within Eqn. 17, resulting in torques that provided the desired curvature.

We ran a simulation with intrinsic curvature $0.02 \text{ radians}/\sigma$, with packing fraction $\phi = 0.3$, filament length $l = 37$, system box length $l_{\text{sys}} = 6.67l$, rigidity $\kappa = 100$, and repulsion $\epsilon^* = 4.65$ (Fig. 15). The filaments coalesce into a single polar band, which then buckles and reassembles at an angle rotated in the direction of filament curvature. This buckling and rotation behavior continues for the length of the simulation, until the band polarization has the opposite orientation that it had initially. The rotation of the polar order vector has been observed in filament gliding assay experiments and simulations of bead-spring filament models with intrinsic curvature [10].

-
- [1] Alberto Montesi, David C. Morse, and Matteo Pasquali. Brownian dynamics algorithm for bead-rod semiflexible chain with anisotropic friction. *The Journal of Chemical Physics*, 122(8):084903, February 2005.
 - [2] Masao Doi and S. F. Edwards. *The Theory of Polymer Dynamics*. Clarendon Press, 1988.
 - [3] Matteo Pasquali and David C. Morse. An efficient algorithm for metric correction forces in simulations of linear polymers with constrained bond lengths. *The Journal of Chemical Physics*, 116(5):1834–1838, February 2002.
 - [4] P. S. Grassia, E. J. Hinch, and L. C. Nitsche. Computer simulations of Brownian motion of complex systems. *Journal of Fluid Mechanics*, 282:373–403, January 1995.
 - [5] Lynn Liu, Erkan Tüzel, and Jennifer L Ross. Loop formation of microtubules during gliding at high density. *Journal of Physics: Condensed Matter*, 23(37):374104, September 2011.
 - [6] Jeffrey M. Moore. Simcore v0.1.2. <http://github.com/jeffmm/simcore.git>, February 2019.
 - [7] Jonathon Anderson, Patrick J. Burns, Daniel Milroy, Peter Ruprecht, Thomas Hauser, and Howard Jay Siegel. Deploying RMACC Summit: An HPC Resource for the Rocky Mountain Region. In *Proceedings of the Practice and Experience in Advanced Research Computing 2017 on Sustainability, Success and Impact*, PEARC17, pages 8:1–8:7, New York, NY, USA, 2017. ACM.
 - [8] Corinna Cortes and Vladimir Vapnik. Support-vector networks. *Machine Learning*, 20(3):273–297, September 1995.
 - [9] Laurens van der Maaten and Geoffrey Hinton. Visualizing Data using t-SNE. *Journal of Machine Learning Research*, 9(Nov):2579–2605, 2008.
 - [10] Kyongwan Kim, Natsuhiko Yoshinaga, Sanjib Bhattacharyya, Hikaru Nakazawa, Mitsuo Umetsu, and Winfried Teizer. Large-scale chirality in an active layer of microtubules and kinesin motor proteins. *Soft Matter*, 14(17):3221–3231, 2018.

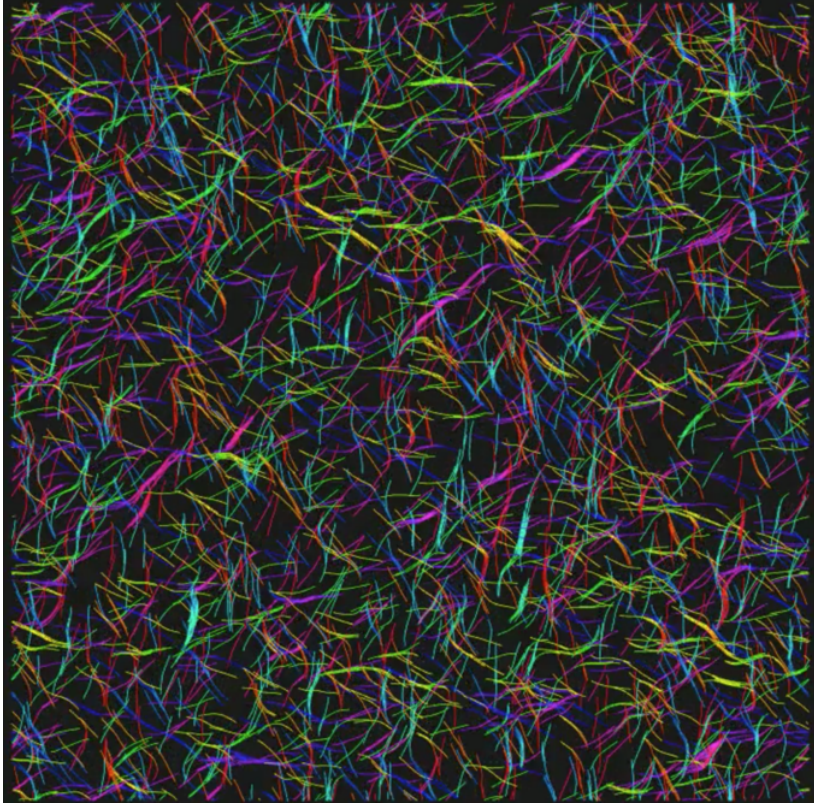


FIG. 5. Movie of simulation with filaments in the active isotropic phase with parameters $\phi = 0.2$, $\kappa = 20$, $\epsilon^* = 1.40$.

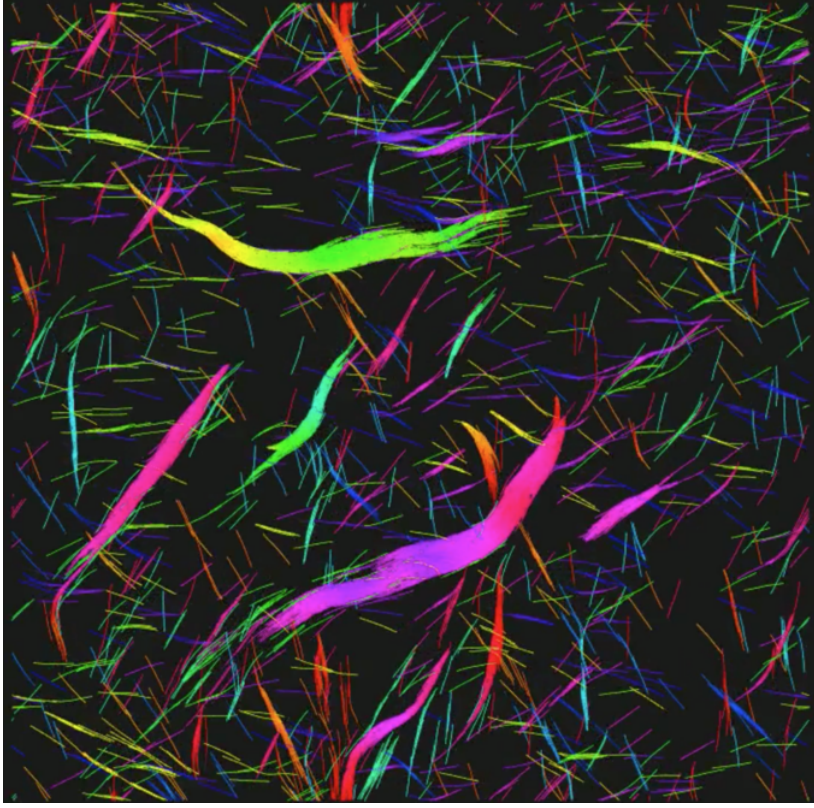


FIG. 6. Movie of simulation with filaments in the flocking phase with parameters $\phi = 0.2$, $\kappa = 100$, $\epsilon^* = 1.86$.

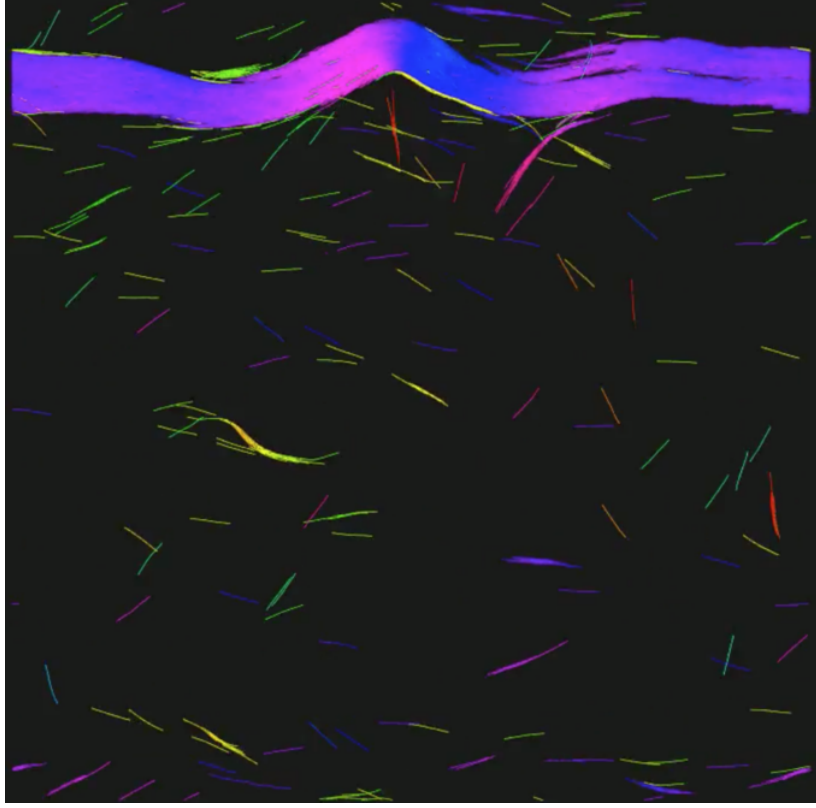


FIG. 7. Movie of simulation with filaments in the polar band phase with parameters $\phi = 0.2$, $\kappa = 100$, $\epsilon^* = 2.79$.

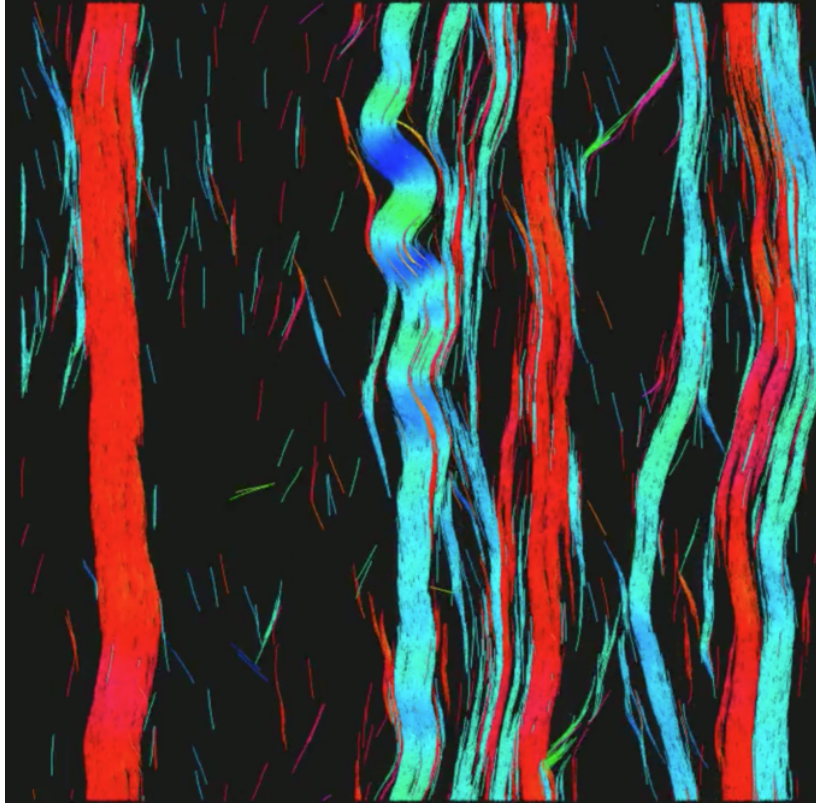


FIG. 8. Movie of simulation with filaments in the nematic band phase with parameters $\phi = 0.4$, $\kappa = 100$, $\epsilon^* = 4.65$.



FIG. 9. Movie of simulation with filaments in the giant flock phase with parameters $\phi = 0.04$, $\kappa = 100$, $\epsilon^* = 4.65$.

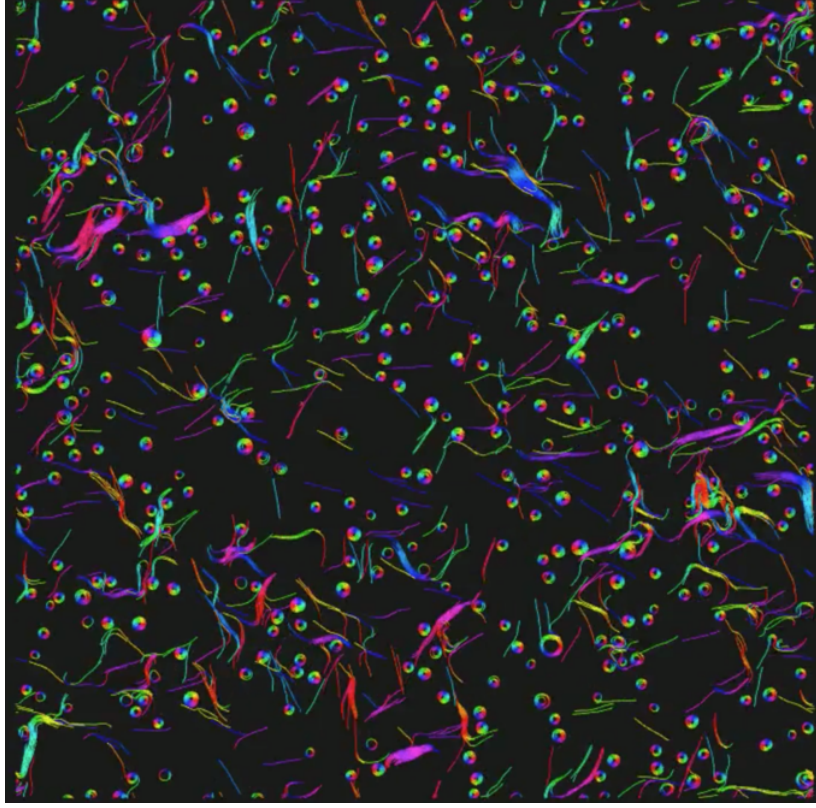


FIG. 10. Movie of simulation with filaments in the spooling phase with parameters $\phi = 0.1$, $\kappa = 20$, $\epsilon^* = 9.31$.

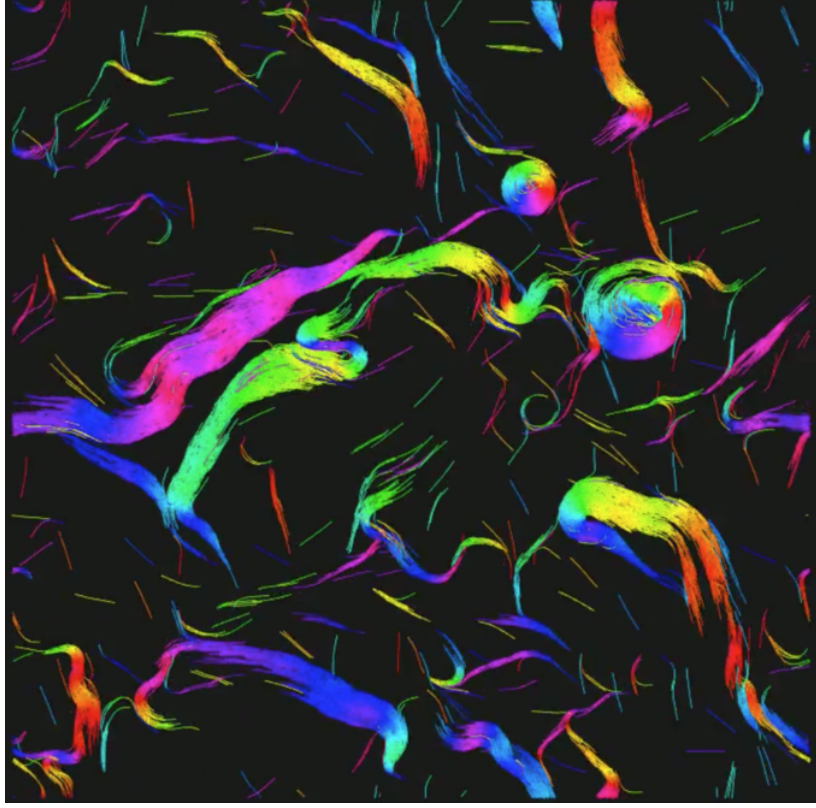


FIG. 11. Movie of simulation with filaments in the swirling phase with parameters $\phi = 0.2$, $\kappa = 100$, $\epsilon^* = 9.31$.

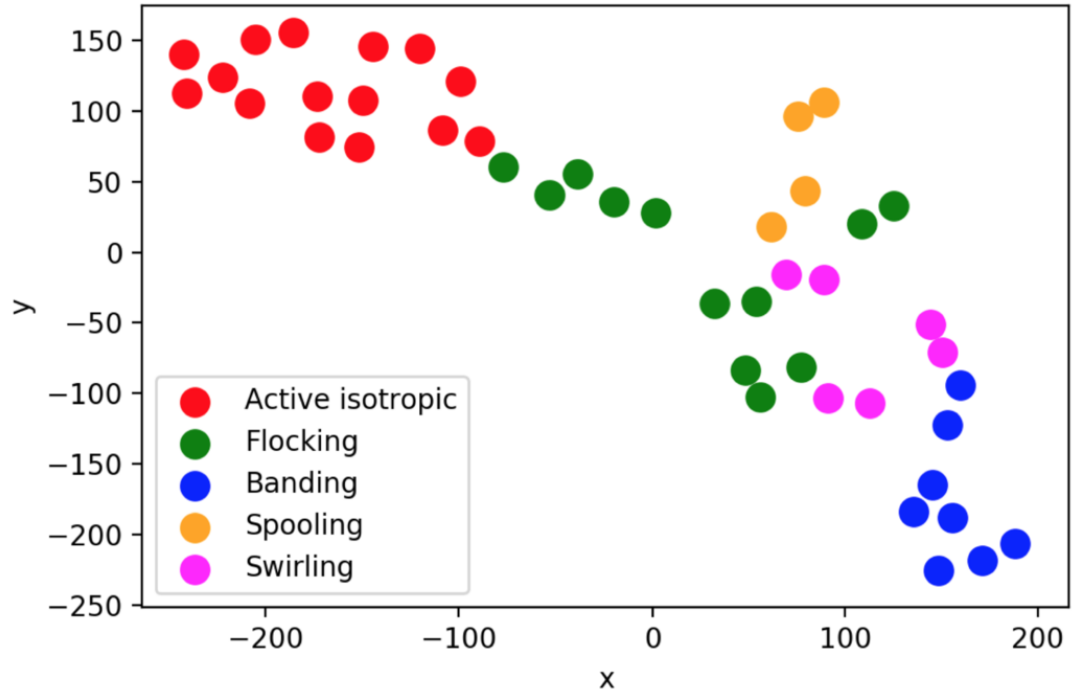


FIG. 12. Individual simulations were categorized and given 6D coordinates according to the six order parameters, then projected onto a 2D plane using a t-distributed Stochastic Neighbor Embedding algorithm resulting in this plot. The projection is a visualization of how the different phases are clustered in six-dimensional order parameter space.

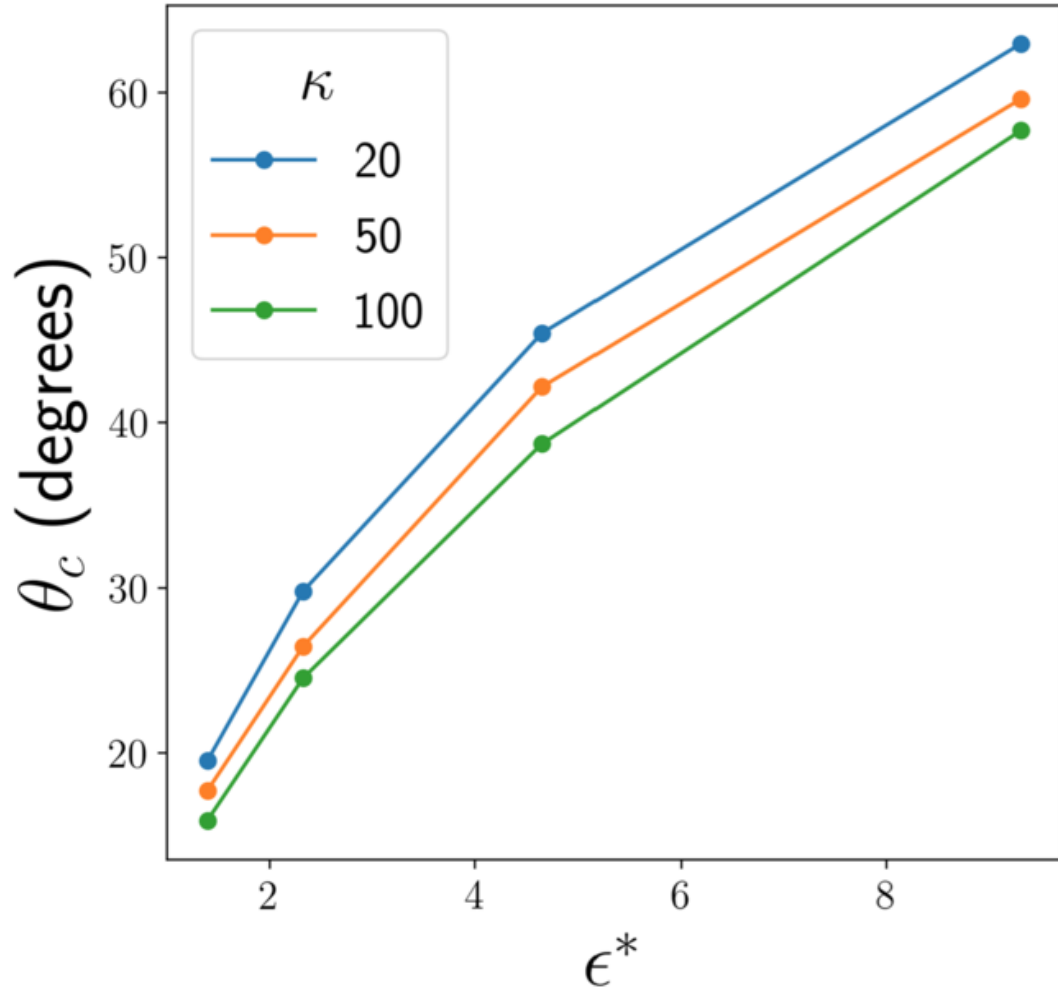


FIG. 13. Critical angle θ_c as function of filament rigidity and repulsion. When two filaments intersect at an angle greater than the critical angle, the filaments will overlap.

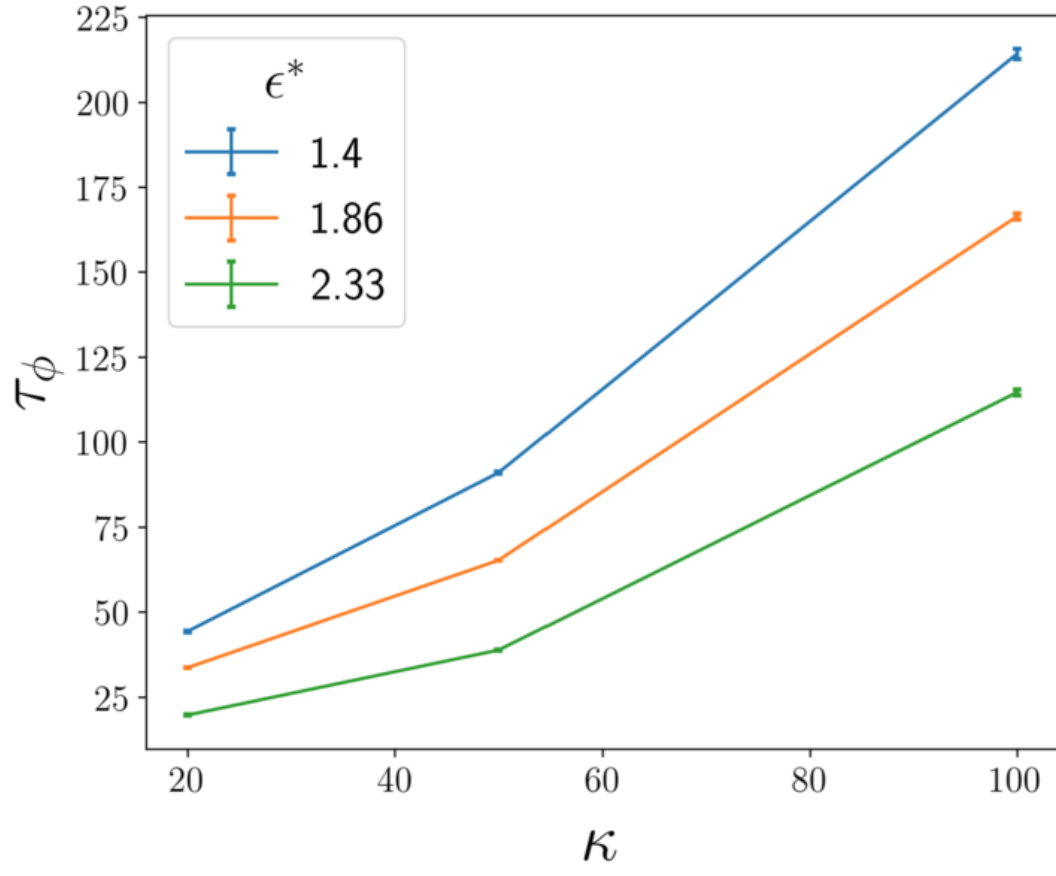


FIG. 14. Orientation autocorrelation lifetime τ_ϕ as function of filament rigidity and repulsion.

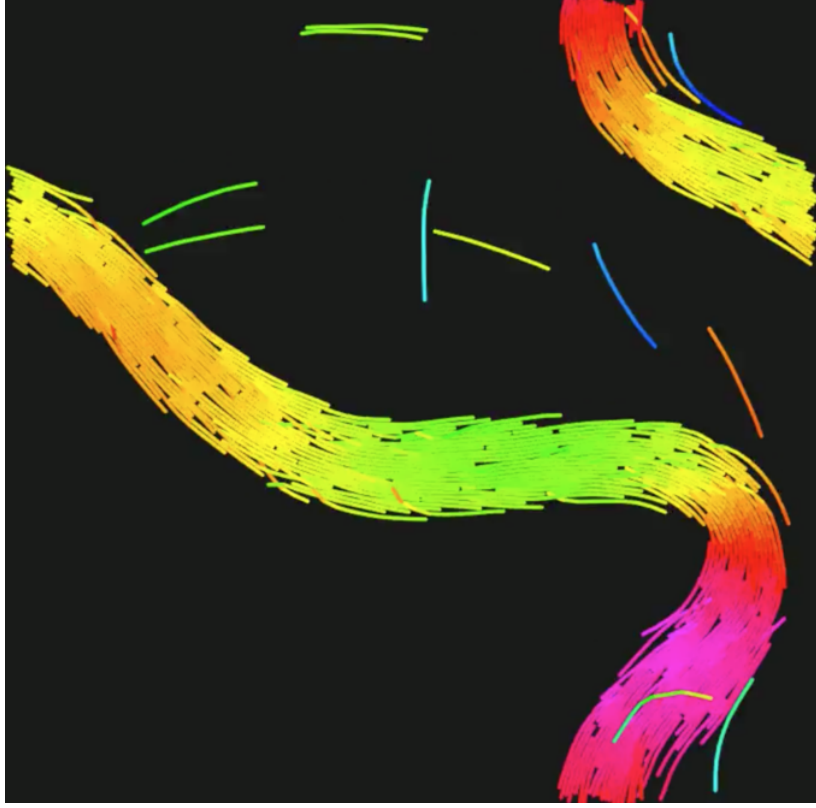


FIG. 15. Movie of simulation with intrinsic curvature $0.02 \text{ rad}/\sigma$ and parameters $\phi = 0.3$, $\kappa = 100$, $\epsilon^* = 4.65$.